

BCAT: A Block Causal Transformer for PDE Foundation Models for Fluid Dynamics

Yuxuan Liu*

Jingmin Sun[†]

Hayden Schaeffer*

Abstract

We introduce BCAT, a PDE foundation model designed for autoregressive prediction of solutions to two dimensional fluid dynamics problems. Our approach uses a block causal transformer architecture to model next frame predictions, leveraging previous frames as contextual priors rather than relying solely on sub-frames or pixel-based inputs commonly used in image generation methods. This block causal framework more effectively captures the spatial dependencies inherent in nonlinear spatiotemporal dynamics and physical phenomena. In an ablation study, next frame prediction demonstrated a 2.9x accuracy improvement over next token prediction. BCAT is trained on a diverse range of fluid dynamics datasets, including incompressible and compressible Navier-Stokes equations across various geometries and parameter regimes, as well as the shallow-water equations. The model’s performance was evaluated on 6 distinct downstream prediction tasks and tested on about 8K trajectories to measure robustness on a variety of fluid dynamics simulations. BCAT achieved an average relative error of 1.92% across all evaluation tasks, outperforming prior approaches on standard benchmarks.

1 Introduction

Fluid mechanics is a fundamental area of study within physics and engineering, describing a wide range of phenomena through modeling of pressure, velocity, and viscosity. It is used in various applications, including climate forecasting, energy generation in wind and hydropower systems, aerodynamics and aircraft design, blood circulation analysis, and more. Due to the highly nonlinear interactions among multiple physical scales, predicting and simulating fluid behavior remains a challenging task. The computational problems become even more difficult in settings with limited observations or noisy measurements. Hence, accurately predicting fluid behavior in such regimes remains a challenge for scientific machine learning.

While foundation models like GPT [8, 32, 33], DALL-E [34, 35], Stable Diffusion [36], LLAMA [46, 47], Phi [1, 2], Gemma [44], and Claude have demonstrated remarkable generalization capabilities in language and vision tasks [6], they have not accurately addressed scientific computing tasks such as simulating partial differential equations (PDEs). These tasks not only require precise predictions but also the ability to learn the underlying physical rules. PDE foundation models aim to address this challenge by using a single deep neural network (DNN) to simultaneously encode and approximate the behavior of a variety of physical models. The objective is to develop a unified DNN capable of predicting multiple physical systems with the ability to simulate solutions in unseen parameter regimes, i.e. out-of-domain predictions. Recent progress in PDE foundation

*Department of Mathematics, UCLA, Los Angeles, CA 90095.

[†]Department of Mathematical Sciences, Carnegie Mellon University, Pittsburgh, PA 15213.

The code is available at: <https://github.com/felix-lyx/bcat>.

models includes the Predicting Operators and Symbolic Expressions (PROSE) [22, 26, 27, 40, 41], Multiple Physics Pretraining (MPP) [30], In-Context Operator Network (ICON) [9, 50, 52, 53], DPOT [17], Fourier Forecasting Network (FourCastNet) [31], Poseidon [19], and Aurora [5].

Main Contributions: One of the key technical components of foundation models is the transformer architecture, known for its ability to efficiently model complex and long-range relationships in data through attention mechanisms. However, current transformer structures utilized in PDE foundation models are hindered by limited context and causality information, since many existing approaches learn to map a fixed window to the next step. In this work, we introduce the **BCAT** model, based on the **B**lock **CA**usal **T**ransformer architecture, adapting the attention mechanism for spatio-temporal dynamics modeling. The BCAT model performs next frame prediction instead of next token prediction, which enhances computational efficiency and allows for more token interactions to capture complex dependencies. Our contributions are listed below.

- We introduce a new PDE foundation model based on a block causal transformer structure for auto-regressive prediction of fluid dynamics. BCAT utilizes next frame prediction to model spatiotemporal context with a 2.9x accuracy improvement over next token predictions. In our experiments, next frame prediction is 185x faster than next token prediction.
- BCAT obtains state-of-the-art accuracy on widely used benchmark datasets: PDEBench (Shallow-water equations, Compressible Navier Stokes, and Incompressible Navier Stokes), PDEArena (Navier Stokes and conditioned Navier Stokes), and CFDBench. Compared to larger SOTA models with 3.4 times the number of parameters than BCAT, BCAT reduces the error by 11%, demonstrating our model’s parameter efficiency. Compared to similarly sized models, BCAT reduces the error by 45%, showing notable accuracy improvements over the current PDE foundation models.

2 Related Works

2.1 PDE Foundation Models

Foundation models are large-scale, pre-trained models that act as flexible bases for a wide range of tasks, leveraging vast amounts of data and computational resources to enable adaptability and generalization across diverse applications [3, 6, 7, 14, 49]. However, their applications to scientific computing are limited, where high precision is needed for numerical tasks. Recently, several approaches have been proposed to explore and develop foundation models for scientific computing. PROSE [22, 26, 27, 40, 41] takes multimodal input to construct solution operators, encoding PDEs as symbolic input to provide additional information and allows zero-shot generalization. ICON [9, 50, 52, 53] uses an in-context learning approach, allowing the model to perform few-shot learning by observing input-output pairs. Some methods focus on the sequential modeling aspect, and various models have been designed to autoregressively predict future states. As additional information is not included, these methods are not able to zero-shot generalize to out-of-distribution data, but can leverage pretraining data to be efficiently fine-tuned [39]. Examples of such models include MPP [30], which uses axial attention to map a fixed context window to future states, and DPOT [17], which uses Fourier attention and stabilizes the autoregressive rollout process through a denoising training process. Poseidon [19] is a swin-transformer-based model, and the model requires fine-tuning for downstream tasks.

2.2 Transformers for Time Series

Time series data takes a similar form as language modeling data, where numerical inputs replace discrete tokens. LLMs and other transformer-based models have been applied to various time series tasks, including forecasting [21], classification [25], and anomaly detection [56]. One key challenge in adapting pretrained transformers for time series forecasting lies in the encoding of numerical data. In [15], scalar time series are encoded as strings, which can be directly processed by pretrained LLMs. In [10], a separate alignment stage is used to allow LLMs to process patched time series. However, as shown in [43], while attention layers can be useful for time series, pretrained LLMs may not outperform simple transformers trained from scratch. Another challenge lies in processing spatio-temporal dynamics, due to the complex interplay between spatial and temporal dependencies. Accurately capturing these interactions often requires models that can handle high-dimensional data, irregular sampling, and non-linear relationships, all while maintaining scalability and computational efficiency. Time-dependent PDEs, climate modeling, and videos can all be seen as examples of spatio-temporal data. The high-dimensional nature requires specific tokenization and processing techniques, such as graph [24] and Fourier mixer [31] for spatial dependencies.

3 Methods

3.1 Problem Setup

Consider parametric families of two-dimensional time-dependent nonlinear PDEs, whose state-variables of interest are represented by $\mathbf{u}(\mathbf{x}, t) \in \mathbb{R}^d$, where d can be up to 4 in our tests, with $\mathbf{x} \in \Omega \subseteq \mathbb{R}^2$. Given data up to T_0 frames, i.e. the sequence:

$$\{\mathbf{u}(\cdot, t_i) \mid 0 \leq i < T_0\},$$

the goal is to predict the subsequent T frames:

$$\{\mathbf{u}(\cdot, t_i) \mid T_0 \leq i < T_0 + T\}.$$

In our experiments, we set $T_0 = T = 10$, that is, 10 frames are given as inputs and the model predicts 10 future frames.

3.2 Model Overview

The BCAT model is illustrated in Figure 1. The model comprises two main components: (1) image tokenization and de-tokenization through patch embedding, and (2) the standard decoder-only transformers similar to GPT-2 [33]. The input data, $\{\mathbf{u}(\cdot, t_i) \mid 0 \leq i < T_0\}$, are first partitioned into patches, which are subsequently flattened and projected into a sequence of visual tokens. The transformer backbone serves as a token mixer, processing these tokens to autoregressively predict future states $\{\mathbf{u}(\cdot, t_i) \mid T_0 \leq i < T_0 + T\}$. We use RMS norm [54] in place of the usual layer norms and find query-key normalization [18] helpful in stabilizing the training process.

Training is performed end-to-end by minimizing the mean squared error between the (normalized) predicted and ground truth sequences. Detailed descriptions of the two components are provided in the following sections.

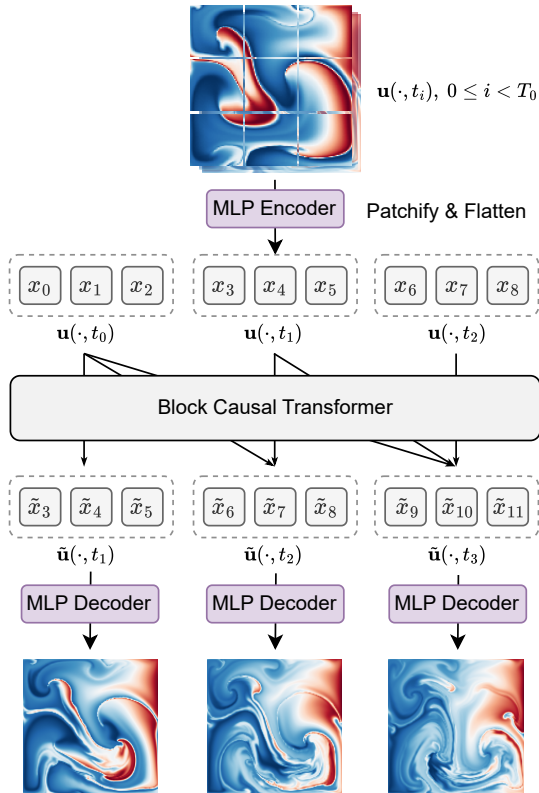


Figure 1: **BCAT model overview.** The inputs to the model are the initial frames sampled from the datasets, which are patchified and converted into a sequence of features. Transformer layers then take the input sequence to perform next frame prediction, where a block causal mask allows spatial interactions within a frame and temporal causality across varying-length context windows. The processed features are then transformed back to form the final predictions.

3.3 Image Tokenization via Patch Embedding

Inspired by [12], we employ a patch embedding layer to convert the input data into a sequence of visual tokens. Each frame in the input data, $\mathbf{u}(\cdot, t_i)$, is first divided into non-overlapping patches, which are then flattened and projected into a sequence of visual tokens. For a maximum of $(T_0 + T)$ data frames, we simply concatenate the visual tokens from each frame to form the input sequence to the transformer backbone.

Let R_x and R_y denote the space resolutions and c be the number of channels (physical fields), i.e., $\mathbf{u}(\cdot, t) \in \mathbb{R}^{R_x \times R_y \times c}$. In the experiments, we fix the spatial resolution to be $R_x = R_y = 128$, consistent with the majority of datasets considered. Data with different spatial resolutions are upsampled via interpolation or downsampled to match this resolution. To unify the number of channels (physical fields) across various PDEs, we zero-pad all input data to $c = 4$ to match the data size with the largest number of channels.

Choosing a patch size of P for each spatial dimension transforms each frame $\mathbf{u}(\cdot, t)$ into $(R_x/P) \times (R_y/P)$ patches, resulting in a sequence of up to $(T_0 + T) \times (R_x/P) \times (R_y/P)$ visual tokens. We observed that the choice of patch size P significantly influences the performance of the

model, which is quantified in Section 4.3. For our model, we select $P = 8$, the smallest size that maintains a reasonable sequence length. This choice results in a maximum sequence length of $(10 + 10) \times (128/8) \times (128/8) = 5120$.

After the transformer backbone, the sequence of tokens is projected back to physical space and then deflattened to reconstruct the predicted future states $\{\mathbf{u}(\cdot, t_i) \mid T_0 \leq i < T_0 + T\}$.

3.4 Preliminary: Next Token Prediction

In both language modeling and autoregressive image generation, next token prediction is the key learning task. For language models, the model predicts the probability distribution of the next token given the previous tokens, enabling the generation of coherent sentences by sampling tokens sequentially [33, 48]. For autoregressive image generation, images are treated as sequences of pixels or patches, with each element predicted based on prior elements in the sequence [11]. Both applications rely on the autoregressive causal property, where future predictions depend only on prior context. More precisely, given a sequence of discrete tokens $X = (x_1, x_2, \dots, x_S)$, the modeling assumption for most language models is that:

$$p(x_1, \dots, x_S) = \prod_{s=1}^S p(x_s | x_1, x_2, \dots, x_{s-1}). \quad (1)$$

This is a reasonable assumption for sentence generation, as language typically follows a left-to-right sequential structure. However, for image generation, such dependencies are not as clear. Unlike text, images exhibit spatial invariance: the pixel/patch in the top-left corner does not inherently depend on the pixel/patch in the bottom-right corner.

3.5 Next Frame Prediction

While the causal property is less intuitive for spatial dependencies, it is a natural assumption for temporal dynamics, especially for Markovian sequences. Next frame prediction is the natural solution that addresses these concerns [9, 51], where visual tokens within the same frame can attend to each other and all tokens for the same frame will be generated in parallel conditioned on previous frames.

Denote the input token sequence as $X = (x_1, \dots, x_S)$ and the BCAT model as f_θ , where $S = (T + T_0) \times N$ is the total sequence length and $N = (R_x/P) \times (R_y/P)$ is the number of tokens per frame. Instead of learning to predict the immediate next token,

$$(x_1, x_2, \dots, x_s) \xrightarrow{f_\theta} (x_2, x_3, \dots, x_{s+1}),$$

the BCAT model learns to predict the next frame given the previous frames:

$$(x_1, x_2, \dots, x_s) \xrightarrow{f_\theta} (x_{N+1}, x_{N+2}, \dots, x_{s+N}).$$

To achieve this, similar to causal masks in transformers to mask out future tokens [48], we use a block lower triangular causal mask [9, 45] to allow spatial dependencies and temporal causality:

$$M = \begin{bmatrix} \mathbf{1}_{N \times N} & \mathbf{0}_{N \times N} & \mathbf{0}_{N \times N} & \dots & \mathbf{0}_{N \times N} \\ \mathbf{1}_{N \times N} & \mathbf{1}_{N \times N} & \mathbf{0}_{N \times N} & \dots & \mathbf{0}_{N \times N} \\ \mathbf{1}_{N \times N} & \mathbf{1}_{N \times N} & \mathbf{1}_{N \times N} & \dots & \mathbf{0}_{N \times N} \\ \vdots & \vdots & \vdots & \ddots & \vdots \\ \mathbf{1}_{N \times N} & \mathbf{1}_{N \times N} & \mathbf{1}_{N \times N} & \dots & \mathbf{1}_{N \times N} \end{bmatrix}. \quad (2)$$

Here $\mathbf{1}_{N \times N}$ and $\mathbf{0}_{N \times N}$ represent constant 1/0 matrices of dimension $N \times N$.

We compare next frame prediction and next token prediction in Section 4.3, showing the accuracy gains from using next frame prediction in the prediction tasks. One additional benefit of next frame prediction over next token prediction is inference efficiency. For inference of autoregressive models, the model needs to be called repeatedly to generate the next token/frame sequentially. For next token prediction, to generate T future frames, the model needs to be called $T \times N$ times, while for next frame prediction, the model only needs to be called T times, providing significant speedup (key-value caching can be used in both cases for further speedup). In our experiments, next frame prediction is 185x faster than next token prediction (see Appendix 4.4).

3.6 Implementation Details

The architecture utilizes a decoder-only transformer similar to GPT-2 [33] and Llama-3 [14]. We use RMS norm [54] in place of layer norms and add query-key normalizations [18] after the attention projections, which we found to help stabilize the training process. In the feedforward network (FFN) of transformer layers, we use SwiGLU activation function [38], and to keep a similar parameter count, the FFN hidden dimension is rescaled to be $\frac{8}{3}$ x the feature dimension instead of the more common 4x. More architecture and training details are included in Appendix B.

4 Experiments

4.1 Experiment Setup

Dataset. The dataset we use consists of 6 parametric families of PDEs that model fluid dynamics in different regimes. We collect the dataset from 3 heterogeneous sources: PDEBench [42], PDEArena [16], and CFDBench [29]. The dataset includes shallow water equations and the Navier-Stokes system with incompressible and compressible flow, regular and complex geometries, and different buoyancy settings. For datasets that do not provide a train/val/test splitting, we use the standard 80%/10%/10% splitting. The total amount of data samples is about 69K trajectory sequences (time homogeneity can be used to create more training input/output pairs), which is the current amount used in comparable models. More details are included in Appendix A.

Evaluation Metric. We use the relative L^2 norm as the evaluation metric. More precisely, given the ground truth \mathbf{u} and model’s prediction $\tilde{\mathbf{u}}$, we compute the (time-averaged) relative L^2 error:

$$\frac{1}{T} \sum_{i=T_0}^{T_0+T-1} \frac{\|\mathbf{u}(\cdot, t_i) - \tilde{\mathbf{u}}(\cdot, t_i)\|_2}{\|\mathbf{u}(\cdot, t_i)\|_2 + \varepsilon}, \quad (3)$$

where $T_0 = 10$ is the number of input steps, $T = 10$ is the number of output steps, and $\varepsilon = 10^{-7}$. Note that for the Navier-Stokes dataset from PDEArena, the temporal grid resolution is only 14, thus we set $T = 4$ for this dataset only. The average used in the last column of Table 1 is the average of the relative L^2 errors over the 6 families, i.e., the average over each row of the table.

Baselines and Comparisons. We evaluate our BCAT model against the following baseline methods. DeepONet [28] and FNO [23] are two widely used single-operator learning techniques designed to efficiently approximate solution operators for PDEs. UNet [37] is a classic convolutional neural network model for image processing, known for its symmetric hierarchical structure that enables it to capture both contextual information and fine details for pixel-wise predictions.

Table 1: **Main Results and Comparisons with Baselines.** The numbers reported are relative L^2 errors (%). The averages are taken with respect to the 6 distinct families listed in the columns of the table.

Model	Param	PDEBench			PDEArena		CFDBench	Average
		SWE	CNS*	INS	NS	NS-cond	-	
DeepONet	3.5M	3.55	7.41	64.61	35.33	51.85	12.50	29.21
FNO	0.6M	3.71	6.31	36.84	38.67	55.63	8.52	24.95
UNet	5.6M	0.33	3.19	3.43	12.56	16.82	0.76	6.18
MPP-B	116M	1.02	1.90	7.52	5.71	12.57	1.23	4.99
MPP-L	407M	0.47	1.53	6.42	4.64	9.64	0.73	3.91
DPOT-M	122M	0.54	1.01	5.20	4.92	8.55	0.64	3.47
ViT	155M	0.25	1.42	2.13	5.54	10.20	0.51	3.34
DPOT-L	523M	0.15	0.89	4.08	2.21	5.29	0.34	2.16
BCAT	156M	0.26	0.61	2.19	2.61	5.15	0.70	1.92

Table 2: **Comparing next frame prediction and next token prediction.** The errors shown are relative L^2 errors (%) for PDEArena NS dataset. *The Next-Token error is computed assuming all previous tokens are exactly known (i.e., the full trajectory is inputted to the model, similar to training time). It is not a standard metric and is only used to provide a comparison.

Method	Param	Testing Error	Training Dataset Error	Next-Token Error*
Next token prediction	156M	7.44	4.34	1.46
Next frame prediction	156M	2.61	1.51	1.39

ViT [13], a transformer-based image processing model, is notable for its ability to capture global dependencies in images and its scalability across various image and video processing tasks. Lastly, two recent PDE foundation models, MPP [30] and DPOT [17]. Both MPP and DPOT autoregressively predict PDE solutions, with MPP based on Axial-ViT and DPOT based on Adaptive Fourier Neural Operators. Additional details about these baselines can be found in Appendix B.3. Note that DeepONet and FNO are designed for single tasks but can be extended to multi-task prediction using fine-tuning [39, 55]. For fairness, all comparisons are performed in a zero-shot fashion.

4.2 Main Results

We present the main results in Table 1, where we report the relative L^2 error (%) for each family of equations and their average. We use the same zero-shot setting for all models: a single model is trained to predict all families of equations without any fine-tuning. The BCAT model achieves the best results on 3 families and the second-best results on the other 3 families. Note that ViT uses a similar structure to BCAT but a different training objective, and achieves the best results on the other 3 families. However, for the more complicated PDEArena datasets where most baselines have higher errors, BCAT outperforms all other models including ViT by a large margin, demonstrating the effectiveness of our proposed model. To demonstrate the efficiency of BCAT, we compare inference speed and GPU memory usage in Section 4.4. We include example visualizations of the BCAT model output in Figure 2, and compare outputs from different models in Figure 3. More visualizations can be found in Appendix C.

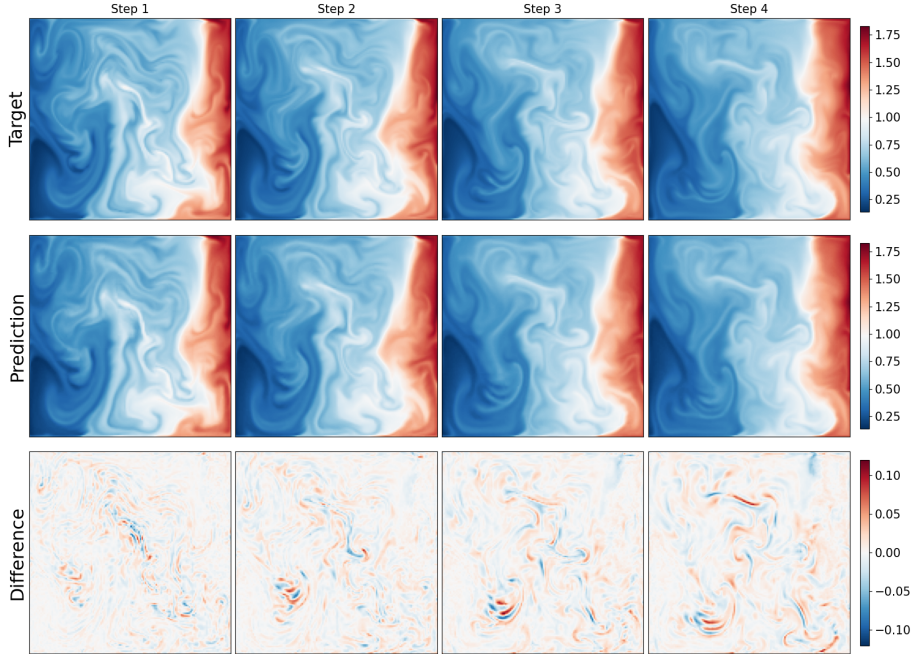


Figure 2: **Example outputs from the BCAT model.** 4 output steps for PDEArena Navier-Stokes dataset. The channel plotted is the particle density in equation (12). Each column represents a different timestamp. For this trajectory, the relative L^2 error is 2.73%.

4.3 Ablation Studies

In this section, we present the results of our ablation studies to validate some key architecture choices.

Next Frame Prediction v.s. Next Token Prediction. We directly compare the performance of BCAT with next frame prediction and next token prediction on the PDEArena NS dataset. We use the same model and training setup for both models, except that the next-token-prediction variant is trained to predict the next token instead of the next frame (and the mask is causal instead of block causal). When trained on a mixture of all 6 families, the next-token-prediction variant fails to converge, so we only train it on the PDEArena NS dataset (the shorter dataset with 14 frames).

The results are shown in Table 2. We observe that the next-frame-prediction model achieves a 2.9x better relative L^2 error compared to the next-token-prediction variant, demonstrating the effectiveness of our proposed training objective. We also compute the error on the training dataset and the “next-token error.” As the PDEArena NS dataset is a relatively small dataset, both models are overfitting to the training dataset to some degree; however, there is a performance difference between the two as shown by the error gap.

The “next-token error” is computed assuming all previous tokens are exactly known (i.e. no prior error). More precisely, during testing time, we input the full trajectory to the model with proper masks to prevent data leaking, similar to training time. Both models are only asked to predict the immediate next token/frame and thus no autoregressive rollout is needed. We are thus measuring the amount of error over one step, i.e., the “local error”. In this case, we observe that the performance of both models are relatively similar. This shows that the two models have similar (local) approximation power, but the next-frame-prediction model is better conditioned for

Table 3: **Comparing the performance of BCAT and Time-then-Space Model.** The errors shown are relative L^2 errors (%).

Model	Param	Average Testing Error
Time-then-Space	206M	1.97
BCAT	156M	1.92

Table 4: **Comparing the performance of BCAT and ViT with different patch size.** The errors shown are relative L^2 errors (%).

Model	Patch Size	Param	Average Testing Error
ViT	16	162M	4.10
ViT	8	155M	3.34
BCAT	32	191M	4.03
BCAT	16	163M	2.64
BCAT	8	156M	1.92

multi-step prediction. Specifically, the next-frame-prediction has a slower accumulation of error rate than the next-token-prediction approach. As discussed in Section 3.5, to autoregressively generate T future frames, the next-frame-prediction model only needs to be recursively called T times, while the next-token-prediction variant needs to be recursively called $T \times N$ times (where N is the number of tokens per frame). This may be the mechanism that leads to a significant reduction in error accumulation for the next-frame-prediction model.

Comparison with Spatio-Temporal Attention. The forward prediction task for 2D fluid dynamics is similar to a video generation task, where the state variable at each timestamp is akin to a frame in the video. In [4], several different forms of self-attention for processing spatial-temporal dynamics are compared for video classification task. Our BCAT model flattens the patches from all frames into a single sequence, and can be seen as a variant of joint space-time self-attention discussed in [4]. Similarly, MPP [30] is a variant of axial self-attention. Another approach that has not appeared in the literature as a backbone to PDE foundation models is the divided space-time self-attention, where temporal attention and spatial attention are separately applied one after the other. We implement this variant and refer to it as the Time-then-Space model. The temporal attention is a causal self-attention and the spatial attention is a full self-attention. All other configurations and hyperparameters are kept the same as the BCAT model. The results are shown in Table 3, where the BCAT model outperforms the spatio-temporal variant. This shows that the joint space-time self-attention is more effective for the forward prediction task.

Effect of Patch Size. In the image tokenization step, the patch size P to divide the image into non-overlapping patches is a key hyperparameter. Note that this is a tradeoff between model complexity and feature spatial resolution, as half the patch size makes the sequence length 4x longer, thus 16x the time complexity and 4x space complexity (assuming memory efficient attention), even though the model parameter size remains similar, since models with smaller patch size have fewer parameters in patch embedding due to smaller dimensions per patch. However, we observe that having a smaller patch size and hence more visual tokens significantly improves the performance for both BCAT and ViT. The results are shown in Table 4.

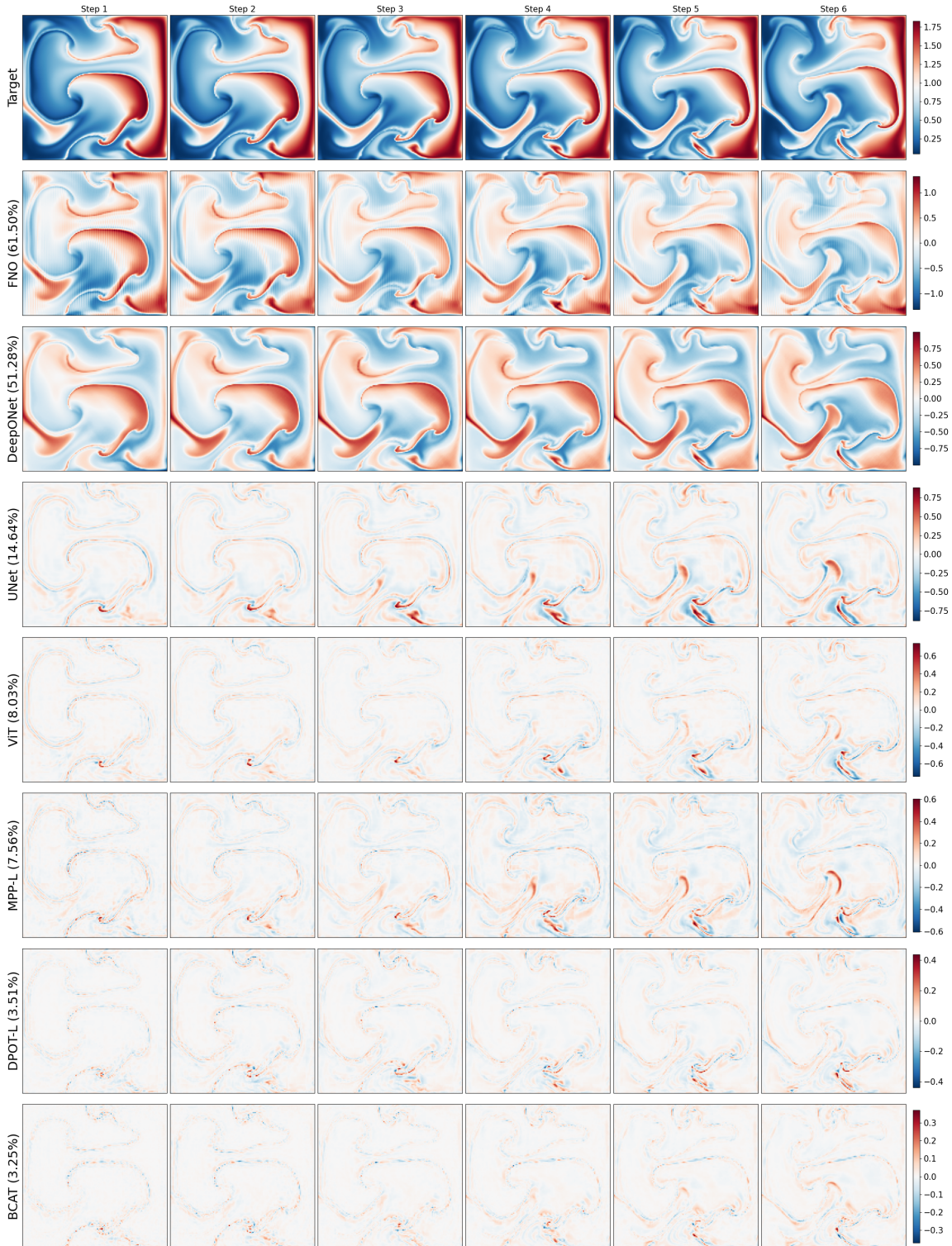


Figure 3: **Comparing outputs from different models.** The target (first row) is the first 6 output steps from the PDEArena Navier-Stokes (conditioned) dataset (particle density channel). For each model (each row), we display the difference between the target and model output. Relative L^2 errors for the full trajectories are listed after the model names.

Table 5: **Additional Ablation Studies.** Each row represents a different variant and we underline the difference with the BCAT model (last row). The errors shown are relative L^2 errors (%).

Activation	QK-Norm	Mask	Param	Average Testing Error
SwiGLU	✗	block causal	155.6M	2.04
SwiGLU	✓	<u>causal</u>	155.6M	3.13
<u>GeLU</u>	✓	block causal	154.8M	2.00
SwiGLU	✓	block causal	155.6M	1.92

Table 6: **Comparing the inference speed and GPU memory usage for all models.** We measure the recourse usage for different models and variants to generate 10 output steps for a single trajectory.

Model	Param	Inference Speed (ms)	GPU Memory Usage (MB)
DeepONet	3.5M	2.7	190
FNO	0.6M	1.7	372
UNet	5.6M	1.3	135
ViT	155M	5.4	2362
MPP-B	116M	207.9	3087
MPP-L	407M	438.3	10869
DPOT-M	122M	95.7	1864
DPOT-L	523M	194.3	7985
Time-then-Space Variant	206M	175.5	3168
Next-token-prediction Variant	156M	13165	2402
BCAT	156M	70.9	2499

Additional Architecture Ablation Study. We validate some architecture details by comparing the average testing error. The results are shown in Table 5. We found query-key normalization [18] helpful in stabilizing the training process, especially towards the end of the training phase. Under similar parameter counts, we found SwiGLU activation function [38] better than GeLU. Note that the parameter count is not exactly the same since the MLP hidden dimension is rounded to the nearest multiple of 64. For the attention mask, to prevent data leaking in next frame prediction, any submask of the block causal mask (2) can work. We compare the BCAT model and a variant using a standard causal mask to perform next frame prediction. We observe that the block causal mask leads to better performance, demonstrating that having more token interactions within the same frame is beneficial for the forward prediction task.

4.4 Resource Usage Comparison

In Table 6, we compare the inference speed and GPU memory usage for all models. To obtain these results, on a single NVIDIA H100 GPU, we use a batch size of 1 and measure the time required to generate 10 output steps for the shallow water equation. To ensure stability, we average run time over 50 repeats after some warmup. While smaller models (FNO, DeepONet, and UNet) have a faster run time, BCAT outperforms all models with comparable or larger sizes except ViT, which shares the same transformer layer without autoregressive rollout.

5 Conclusion

In this work, we introduced BCAT, a novel PDE foundation model designed for autoregressive prediction of fluid dynamics solutions. Leveraging a block causal transformer architecture, BCAT addresses the limitations of existing models by focusing on next frame prediction rather than next token prediction. This design captures the complex spatiotemporal dependencies inherent in fluid dynamics more effectively, leading to improved accuracy and computational efficiency. Our experimental results highlight the strengths of BCAT in various popular benchmark datasets, including PDEBench, PDEArena, and CFDBench. BCAT consistently outperformed state-of-the-art models across diverse evaluation tasks. Notably, BCAT demonstrated superior parameter efficiency, outperforming larger models with 3.4 times more parameters, and achieved notable improvements over similarly sized models. The ablation study further validated the advantages of next frame prediction approach, which enhanced accuracy and efficiency in modeling nonlinear physical phenomena in fluid dynamics. This finding underscores the effectiveness of the block causal framework in capturing complex dependencies. BCAT represents a significant step forward in the development of PDE foundation models, providing a powerful and efficient tool for advancing scientific computing and fluid dynamics research.

Acknowledgments

Yuxuan Liu and Hayden Schaeffer are supported in part by NSF DMS 2427558.

References

- [1] Marah Abdin, Jyoti Aneja, Hany Awadalla, Ahmed Awadallah, Ammar Ahmad Awan, Nguyen Bach, Amit Bahree, Arash Bakhtiari, Jianmin Bao, Harkirat Behl, et al. Phi-3 technical report: A highly capable language model locally on your phone. *arXiv preprint arXiv:2404.14219*, 2024.
- [2] Marah Abdin, Jyoti Aneja, Harkirat Behl, Sébastien Bubeck, Ronen Eldan, Suriya Gunasekar, Michael Harrison, Russell J Hewett, Mojan Javaheripi, Piero Kauffmann, et al. Phi-4 technical report. *arXiv preprint arXiv:2412.08905*, 2024.
- [3] Josh Achiam, Steven Adler, Sandhini Agarwal, Lama Ahmad, Ilge Akkaya, Florencia Leoni Aleman, Diogo Almeida, Janko Altschmidt, Sam Altman, Shyamal Anadkat, et al. Gpt-4 technical report. *arXiv preprint arXiv:2303.08774*, 2023.
- [4] Gedas Bertasius, Heng Wang, and Lorenzo Torresani. Is space-time attention all you need for video understanding? In *ICML*, volume 2, page 4, 2021.
- [5] Cristian Bodnar, Wessel P Bruinsma, Ana Lucic, Megan Stanley, Johannes Brandstetter, Patrick Garvan, Maik Riechert, Jonathan Weyn, Haiyu Dong, Anna Vaughan, et al. Aurora: A foundation model of the atmosphere. *arXiv preprint arXiv:2405.13063*, 2024.
- [6] Rishi Bommasani, Drew A Hudson, Ehsan Adeli, Russ Altman, Simran Arora, Sydney von Arx, Michael S Bernstein, Jeannette Bohg, Antoine Bosselut, Emma Brunskill, et al. On the opportunities and risks of foundation models. *arXiv preprint arXiv:2108.07258*, 2021.
- [7] Tim Brooks, Bill Peebles, Connor Holmes, Will DePue, Yufei Guo, Li Jing, David Schnurr, Joe Taylor, Troy Luhman, Eric Luhman, et al. Video generation models as world simulators, 2024.

- [8] Tom Brown, Benjamin Mann, Nick Ryder, Melanie Subbiah, Jared D Kaplan, Prafulla Dhariwal, Arvind Neelakantan, Pranav Shyam, Girish Sastry, Amanda Askell, et al. Language models are few-shot learners. *Advances in neural information processing systems*, 33:1877–1901, 2020.
- [9] Yadi Cao, Yuxuan Liu, Liu Yang, Rose Yu, Hayden Schaeffer, and Stanley Osher. Vicon: Vision in-context operator networks for multi-physics fluid dynamics prediction. *arXiv preprint arXiv:2411.16063*, 2024.
- [10] Ching Chang, Wei-Yao Wang, Wen-Chih Peng, and Tien-Fu Chen. Llm4ts: Aligning pre-trained llms as data-efficient time-series forecasters. *arXiv preprint arXiv:2308.08469*, 2024.
- [11] Mark Chen, Alec Radford, Rewon Child, Jeffrey Wu, Heewoo Jun, David Luan, and Ilya Sutskever. Generative pretraining from pixels. In *International conference on machine learning*, pages 1691–1703. PMLR, 2020.
- [12] Alexey Dosovitskiy, Lucas Beyer, Alexander Kolesnikov, Dirk Weissenborn, Xiaohua Zhai, Thomas Unterthiner, Mostafa Dehghani, Matthias Minderer, Georg Heigold, Sylvain Gelly, Jakob Uszkoreit, and Neil Houlsby. An image is worth 16x16 words: Transformers for image recognition at scale. In *International Conference on Learning Representations*, 2021.
- [13] Alexey Dosovitskiy, Lucas Beyer, Alexander Kolesnikov, Dirk Weissenborn, Xiaohua Zhai, Thomas Unterthiner, Mostafa Dehghani, Matthias Minderer, Georg Heigold, Sylvain Gelly, Jakob Uszkoreit, and Neil Houlsby. An image is worth 16x16 words: Transformers for image recognition at scale. *ICLR*, 2021.
- [14] Abhimanyu Dubey, Abhinav Jauhri, Abhinav Pandey, Abhishek Kadian, Ahmad Al-Dahle, Aiesha Letman, Akhil Mathur, Alan Schelten, Amy Yang, Angela Fan, et al. The llama 3 herd of models. *arXiv preprint arXiv:2407.21783*, 2024.
- [15] Nate Gruver, Marc Finzi, Shikai Qiu, and Andrew G Wilson. Large language models are zero-shot time series forecasters. *Advances in Neural Information Processing Systems*, 36, 2024.
- [16] Jayesh K Gupta and Johannes Brandstetter. Towards multi-spatiotemporal-scale generalized pde modeling. *arXiv preprint arXiv:2209.15616*, 2022.
- [17] Zhongkai Hao, Chang Su, Songming Liu, Julius Berner, Chengyang Ying, Hang Su, Anima Anandkumar, Jian Song, and Jun Zhu. Dpot: Auto-regressive denoising operator transformer for large-scale pde pre-training. *arXiv preprint arXiv:2403.03542*, 2024.
- [18] Alex Henry, Prudhvi Raj Dachapally, Shubham Pawar, and Yuxuan Chen. Query-key normalization for transformers. *arXiv preprint arXiv:2010.04245*, 2020.
- [19] Maximilian Herde, Bogdan Raonić, Tobias Rohner, Roger Käppeli, Roberto Molinaro, Emmanuel de Bézenac, and Siddhartha Mishra. Poseidon: Efficient foundation models for pdes. *arXiv preprint arXiv:2405.19101*, 2024.
- [20] Shengding Hu, Yuge Tu, Xu Han, Chaoqun He, Ganqu Cui, Xiang Long, Zhi Zheng, Yewei Fang, Yuxiang Huang, Weilin Zhao, et al. Minicpm: Unveiling the potential of small language models with scalable training strategies. *arXiv preprint arXiv:2404.06395*, 2024.
- [21] Ming Jin, Shiyu Wang, Lintao Ma, Zhixuan Chu, James Y Zhang, Xiaoming Shi, Pin-Yu Chen, Yuxuan Liang, Yuan-Fang Li, Shirui Pan, et al. Time-llm: Time series forecasting by reprogramming large language models. *arXiv preprint arXiv:2310.01728*, 2023.

- [22] Derek Jollie, Jingmin Sun, Zecheng Zhang, and Hayden Schaeffer. Time-series forecasting, knowledge distillation, and refinement within a multimodal pde foundation model. *arXiv preprint arXiv:2409.11609*, 2024.
- [23] Zongyi Li, Nikola Kovachki, Kamyar Azizzadenesheli, Burigede Liu, Kaushik Bhattacharya, Andrew Stuart, and Anima Anandkumar. Fourier neural operator for parametric partial differential equations. *arXiv preprint arXiv:2010.08895*, 2020.
- [24] Lei Liu, Shuo Yu, Runze Wang, Zhenxun Ma, and Yanming Shen. How can large language models understand spatial-temporal data? *arXiv preprint arXiv:2401.14192*, 2024.
- [25] Minghao Liu, Shengqi Ren, Siyuan Ma, Jiahui Jiao, Yizhou Chen, Zhiguang Wang, and Wei Song. Gated transformer networks for multivariate time series classification. *arXiv preprint arXiv:2103.14438*, 2021.
- [26] Yuxuan Liu, Jingmin Sun, Xinjie He, Griffin Pinney, Zecheng Zhang, and Hayden Schaeffer. Prose-fd: A multimodal pde foundation model for learning multiple operators for forecasting fluid dynamics. *arXiv preprint arXiv:2409.09811*, 2024.
- [27] Yuxuan Liu, Zecheng Zhang, and Hayden Schaeffer. Prose: Predicting multiple operators and symbolic expressions using multimodal transformers. *Neural Networks*, 180:106707, 2024.
- [28] Lu Lu, Pengzhan Jin, and George Em Karniadakis. Deeponet: Learning nonlinear operators for identifying differential equations based on the universal approximation theorem of operators. *arXiv preprint arXiv:1910.03193*, 2019.
- [29] Yining Luo, Yingfa Chen, and Zhen Zhang. Cfdbench: A comprehensive benchmark for machine learning methods in fluid dynamics. *arXiv preprint arXiv:2310.05963*, 2023.
- [30] Michael McCabe, Bruno Régaldo-Saint Blancard, Liam Holden Parker, Ruben Ohana, Miles Cranmer, Alberto Bietti, Michael Eickenberg, Siavash Golkar, Geraud Krawezik, Francois Lanusse, et al. Multiple physics pretraining for physical surrogate models. *arXiv preprint arXiv:2310.02994*, 2023.
- [31] Jaideep Pathak, Shashank Subramanian, Peter Harrington, Sanjeev Raja, Ashesh Chattopadhyay, Morteza Mardani, Thorsten Kurth, David Hall, Zongyi Li, Kamyar Azizzadenesheli, et al. Fourcastnet: A global data-driven high-resolution weather model using adaptive fourier neural operators. *arXiv preprint arXiv:2202.11214*, 2022.
- [32] Alec Radford, Karthik Narasimhan, Tim Salimans, Ilya Sutskever, et al. Improving language understanding by generative pre-training. 2018.
- [33] Alec Radford, Jeff Wu, Rewon Child, David Luan, Dario Amodei, and Ilya Sutskever. Language models are unsupervised multitask learners. 2019.
- [34] Aditya Ramesh, Prafulla Dhariwal, Alex Nichol, Casey Chu, and Mark Chen. Hierarchical text-conditional image generation with clip latents. *arXiv preprint arXiv:2204.06125*, 1(2):3, 2022.
- [35] Aditya Ramesh, Mikhail Pavlov, Gabriel Goh, Scott Gray, Chelsea Voss, Alec Radford, Mark Chen, and Ilya Sutskever. Zero-shot text-to-image generation. In *International conference on machine learning*, pages 8821–8831. Pmlr, 2021.
- [36] Robin Rombach, Andreas Blattmann, Dominik Lorenz, Patrick Esser, and Björn Ommer. High-resolution image synthesis with latent diffusion models. In *Proceedings of the IEEE/CVF conference on computer vision and pattern recognition*, pages 10684–10695, 2022.

- [37] Olaf Ronneberger, Philipp Fischer, and Thomas Brox. U-net: Convolutional networks for biomedical image segmentation. In *Medical image computing and computer-assisted intervention–MICCAI 2015: 18th international conference, Munich, Germany, October 5-9, 2015, proceedings, part III 18*, pages 234–241. Springer, 2015.
- [38] Noam Shazeer. Glu variants improve transformer. *arXiv preprint arXiv:2002.05202*, 2020.
- [39] Shashank Subramanian, Peter Harrington, Kurt Keutzer, Wahid Bhimji, Dmitriy Morozov, Michael W Mahoney, and Amir Gholami. Towards foundation models for scientific machine learning: Characterizing scaling and transfer behavior. *Advances in Neural Information Processing Systems*, 36, 2024.
- [40] Jingmin Sun, Yuxuan Liu, Zecheng Zhang, and Hayden Schaeffer. Towards a foundation model for partial differential equation: Multi-operator learning and extrapolation. *arXiv preprint arXiv:2404.12355*, 2024.
- [41] Jingmin Sun, Zecheng Zhang, and Hayden Schaeffer. Lemon: Learning to learn multi-operator networks. *arXiv preprint arXiv:2408.16168*, 2024.
- [42] Makoto Takamoto, Timothy Praditia, Raphael Leiteritz, Daniel MacKinlay, Francesco Alesiani, Dirk Pflüger, and Mathias Niepert. Pdebench: An extensive benchmark for scientific machine learning. *Advances in Neural Information Processing Systems*, 35:1596–1611, 2022.
- [43] Mingtian Tan, Mike A Merrill, Vinayak Gupta, Tim Althoff, and Thomas Hartvigsen. Are language models actually useful for time series forecasting? In *The Thirty-eighth Annual Conference on Neural Information Processing Systems*, 2024.
- [44] Gemma Team, Morgane Riviere, Shreya Pathak, Pier Giuseppe Sessa, Cassidy Hardin, Surya Bhupatiraju, Léonard Hussenot, Thomas Mesnard, Bobak Shahriari, Alexandre Ramé, et al. Gemma 2: Improving open language models at a practical size. *arXiv preprint arXiv:2408.00118*, 2024.
- [45] Keyu Tian, Yi Jiang, Zehuan Yuan, Bingyue Peng, and Liwei Wang. Visual autoregressive modeling: Scalable image generation via next-scale prediction. *arXiv preprint arXiv:2404.02905*, 2024.
- [46] Hugo Touvron, Thibaut Lavril, Gautier Izacard, Xavier Martinet, Marie-Anne Lachaux, Timothée Lacroix, Baptiste Rozière, Naman Goyal, Eric Hambro, Faisal Azhar, et al. Llama: Open and efficient foundation language models. *arXiv preprint arXiv:2302.13971*, 2023.
- [47] Hugo Touvron, Louis Martin, Kevin Stone, Peter Albert, Amjad Almahairi, Yasmine Babaei, Nikolay Bashlykov, Soumya Batra, Prajjwal Bhargava, Shruti Bhosale, et al. Llama 2: Open foundation and fine-tuned chat models. *arXiv preprint arXiv:2307.09288*, 2023.
- [48] Ashish Vaswani, Noam Shazeer, Niki Parmar, Jakob Uszkoreit, Llion Jones, Aidan N. Gomez, Łukasz Kaiser, and Illia Polosukhin. Attention is all you need. In *Proceedings of the 31st International Conference on Neural Information Processing Systems*, 2017.
- [49] An Yang, Baosong Yang, Beichen Zhang, Binyuan Hui, Bo Zheng, Bowen Yu, Chengyuan Li, Dayiheng Liu, Fei Huang, Haoran Wei, et al. Qwen2. 5 technical report. *arXiv preprint arXiv:2412.15115*, 2024.
- [50] Liu Yang, Siting Liu, Tingwei Meng, and Stanley J Osher. In-context operator learning with data prompts for differential equation problems. *Proceedings of the National Academy of Sciences*, 120(39):e2310142120, 2023.

- [51] Liu Yang, Siting Liu, and Stanley J Osher. Fine-tune language models as multi-modal differential equation solvers. *arXiv preprint arXiv:2308.05061*, 2023.
- [52] Liu Yang, Tingwei Meng, Siting Liu, and Stanley J Osher. Prompting in-context operator learning with sensor data, equations, and natural language. *arXiv preprint arXiv:2308.05061*, 2023.
- [53] Liu Yang and Stanley J Osher. Pde generalization of in-context operator networks: A study on 1d scalar nonlinear conservation laws. *arXiv preprint arXiv:2401.07364*, 2024.
- [54] Biao Zhang and Rico Sennrich. Root mean square layer normalization. *Advances in Neural Information Processing Systems*, 32, 2019.
- [55] Zecheng Zhang, Christian Moya, Lu Lu, Guang Lin, and Hayden Schaeffer. Deeponet as a multi-operator extrapolation model: Distributed pretraining with physics-informed fine-tuning. *arXiv preprint arXiv:2411.07239*, 2024.
- [56] Zihao Zhou and Rose Yu. Can llms understand time series anomalies? *arXiv preprint arXiv:2410.05440*, 2024.

A Dataset Details

The data was obtained from the PDEBench [42], PDEArena [16], and CFDBench [29] datasets. Unless otherwise specified, the space resolution is 128×128 .

A.1 PDEBench [42]

Shallow Water Equation. The quantity of interest is the water depth $h(\mathbf{x}, t)$ on domain $[-2.5, 2.5]^2 \times [0, 1]$ with Neumann boundary condition. The temporal resolution is 101. The equations are:

$$\partial_t h + \nabla h \mathbf{u} = 0, \quad (4)$$

$$\partial_t h \mathbf{u} + \nabla \left(h \mathbf{u} \cdot \mathbf{u} + \frac{1}{2} g_r h^2 \right) = -g_r h \nabla b. \quad (5)$$

Incompressible Navier-Stokes Equation. The quantities of interest are the velocities $\mathbf{u}(\mathbf{x}, t)$ and particle density $c(\mathbf{x}, t)$ on domain $[0, 1]^2 \times [0, 5]$ with Dirichlet boundary condition. The temporal resolution is 1000. The equations are:

$$\rho(\partial_t \mathbf{u} + \mathbf{u} \cdot \nabla \mathbf{u}) = -\nabla p + \mu \Delta \mathbf{u} + \mathbf{F}, \quad (6)$$

$$\nabla \cdot \mathbf{u} = 0, \quad (7)$$

$$\partial_t c + \nabla \cdot (c \mathbf{u}) = 0. \quad (8)$$

The forcing term \mathbf{F} is randomly sampled.

Compressible Navier-Stokes Equation. The quantities of interest are the velocities $\mathbf{u}(\mathbf{x}, t)$, pressure $p(\mathbf{x}, t)$, and density $\rho(\mathbf{x}, t)$ on domain $[0, 1]^2 \times [0, 1]$ with periodic boundary conditions. The temporal resolution is 21. For equations with low viscosities, the dataset is provided on a finer 512×512 space grid, which is downsampled to 128×128 for consistency (through average pooling). The equations are:

$$\partial_t \rho + \nabla \cdot (\rho \mathbf{u}) = 0, \quad (9)$$

$$\rho(\partial_t \mathbf{u} + \mathbf{u} \cdot \nabla \mathbf{u}) = -\nabla p + \eta \Delta \mathbf{u} + (\zeta + \eta/3) \nabla (\nabla \cdot \mathbf{u}), \quad (10)$$

$$\partial_t \left(\varepsilon + \frac{\rho u^2}{2} \right) = -\nabla \cdot \left(\left(\varepsilon + p + \frac{\rho u^2}{2} \right) \mathbf{u} - \mathbf{u} \cdot \sigma' \right). \quad (11)$$

A.2 PDEArena [16]

Incompressible Navier-Stokes Equation. The quantities of interest are the velocities $\mathbf{u}(\mathbf{x}, t)$ and particle density $c(\mathbf{x}, t)$ on domain $[0, 32]^2 \times [18, 102]$ with Dirichlet boundary conditions for velocity and Neumann boundary condition for particle field. The temporal resolution is 14. The equations are:

$$\rho(\partial_t \mathbf{u} + \mathbf{u} \cdot \nabla \mathbf{u}) = -\nabla p + \mu \Delta \mathbf{u} + \mathbf{F}, \quad (12)$$

$$\nabla \cdot \mathbf{u} = 0, \quad (13)$$

$$\partial_t c + \nabla \cdot (c \mathbf{u}) = 0. \quad (14)$$

The forcing term \mathbf{F} takes the form $\mathbf{F} = (0, f)$ with $f = 0.5$.

Incompressible Navier-Stokes Equation (Conditioned). The quantities of interest are the velocities $\mathbf{u}(\mathbf{x}, t)$ and particle density $c(\mathbf{x}, t)$ on domain $[0, 32]^2 \times [18, 102]$ with Dirichlet boundary conditions for velocity and Neumann boundary condition for particle field. The temporal resolution is 56. The equations are:

$$\rho(\partial_t \mathbf{u} + \mathbf{u} \cdot \nabla \mathbf{u}) = -\nabla p + \mu \Delta \mathbf{u} + \mathbf{F}, \quad (15)$$

$$\nabla \cdot \mathbf{u} = 0, \quad (16)$$

$$\partial_t c + \nabla \cdot (c\mathbf{u}) = 0. \quad (17)$$

The forcing term \mathbf{F} takes the form $\mathbf{F} = (0, f)$ where f is uniformly sampled in $[0.2, 0.5]$.

A.3 CFDBench [29]

Incompressible Navier-Stokes Equation. The quantities of interest are the velocities $\mathbf{u}(\mathbf{x}, t)$ and pressure $p(\mathbf{x}, t)$. This dataset contains irregular geometries with Dirichlet boundary conditions. The raw space resolution is 64×64 which is upsampled to 128×128 via interpolation. The equations are:

$$\rho(\partial_t \mathbf{u} + \mathbf{u} \cdot \nabla \mathbf{u}) = -\nabla p + \mu \Delta \mathbf{u}, \quad (18)$$

$$\nabla \cdot \mathbf{u} = 0. \quad (19)$$

B Experiment Details

B.1 Training

We perform data normalization during the training process. Given the input sequence of data $\{\mathbf{u}(\cdot, t_i) \mid 0 \leq i < T_0\}$, we compute the mean and standard deviation of each input trajectory, which are used to normalize both the input and ground truth sequence. The loss function is the standard mean squared error in the normalized space. The models are trained using the AdamW optimizer with a global batch size of 128 for 40 epochs where each epoch is 4,000 steps. The warmup-stable-decay learning rate scheduler [20] is used with 5% warmup and 10% decay. We use learning rate 10^{-3} and weight decay 10^{-4} . On four NVIDIA H100 GPUs, the training takes about 59 hours.

B.2 Model Hyperparameters

We summarize the model hyperparameters in Table 7. An illustration of a transformer layer used in BCAT model is shown in Figure 4.

Table 7: **Model hyperparameters.** FFN means feedforward network.

Hidden dimension - attention	1024	Hidden dimension - FFN	2752
Number of attention heads	8	Number of layers	12
Activation	SwiGLU	Dropout	0
Patch Size	8		

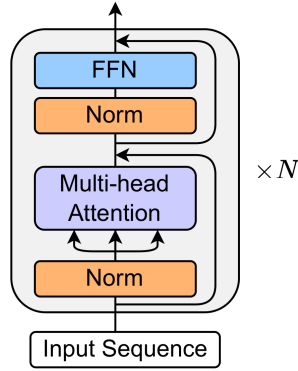


Figure 4: Transformer Layers used in BCAT model.

B.3 Baselines and Comparisons

In this section, we include more details about the compared models.

DeepONet [28]. We employ the unstacked DeepONet architecture, consisting of a single trunk network and a single branch network. Initially, the input data is divided into 8×8 patches, with each patch being embedded into a 128-dimensional vector. These vectors are then passed through the branch network, producing an output with a basis dimension of $p = 50$. Simultaneously, the query point is processed through the trunk network, which also outputs a vector with the same dimension, p . The output solution at the query point is obtained by taking the inner product of the outputs from the two networks.

FNO [23]. We use 4 layers of standard 3d FNO to process the input data. The number of modes to keep in each dimension is set to 8, and the number of hidden channels is set to 16. The 3d FNO model directly maps 10 input steps to 10 output steps.

UNet [37]. We use 8 layers of 3d UNet with GeLU activation and 32 hidden dimensions. The 3d UNet model directly maps 10 input steps to 10 output steps (Padding is added to the input to make it a power of 2, which is needed for the shrinkage in dimension).

ViT [13]. For ViT, we use 12 transformer layers similar to the one shown in Figure 4. The patch size is set to be 8, the hidden dimension for attention is 1024, the hidden dimension for the feedforward network is 4096 with GeLU activation, and the number of heads is 8. The ViT model directly maps 10 input steps to 10 output steps.

MPP [30]. In [30], MPP is trained on a different training dataset and different evaluation metrics are used. For a fair comparison, we retrained MPP-B and MPP-L on our training dataset keeping the same model configurations and optimizer hyperparameters. We evaluate MPP-B and MPP-L using the same testing setup and metric, where rollout is used to obtain all 10 output steps.

DPOT [17]. In [17], DPOT is trained on a different training dataset and different evaluation metrics are used. For a fair comparison, we retrained DPOT-M and DPOT-L on our training dataset keeping the same model configurations and optimizer hyperparameters. We evaluate

DPOT-M and DPOT-L using the same testing setup and metric, where rollout is used to obtain all 10 output steps.

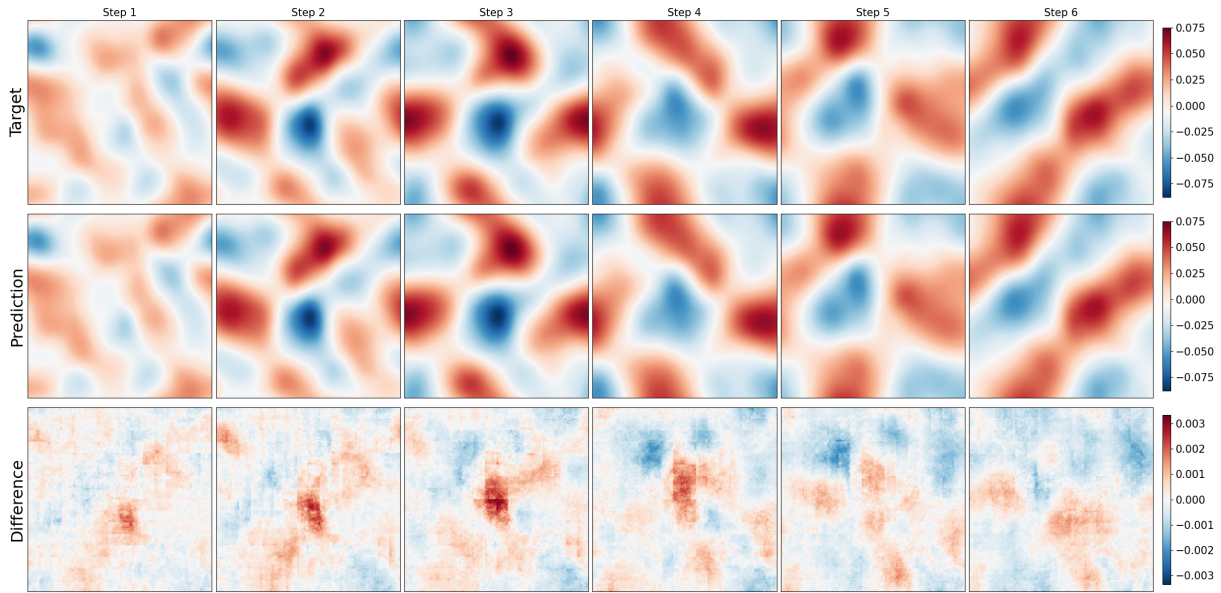
C More Visualizations

C.1 BCAT Model Output Visualizations

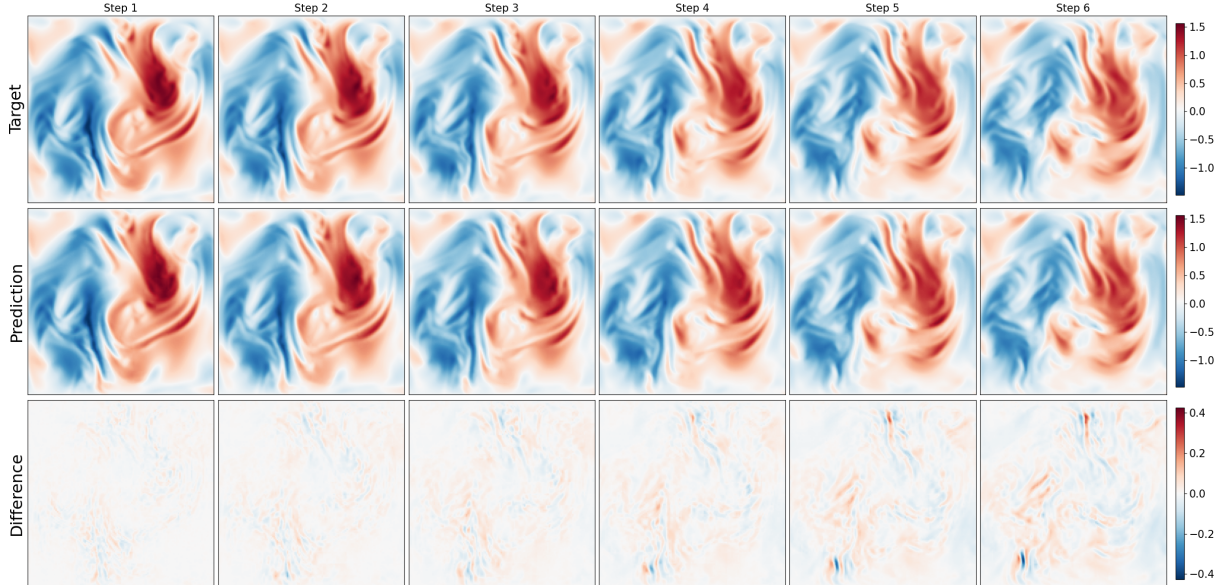
We include more outputs from the BCAT model, see Figure 5.

C.2 Comparing Different Model Outputs

We include more examples comparing different model outputs, see Figure 6.



(a) 6 output steps for PDEBench Compressible Navier-Stokes dataset. The channel plotted is the x -velocity in equation (9). Each column represents a different timestamp. For this trajectory, the relative L^2 error is 0.15%.



(b) 6 output steps for PDEArena Navier-Stokes (conditioned) dataset. The channel plotted is the x -velocity in equation (12). Each column represents a different timestamp. For this trajectory, the relative L^2 error is 5.85%.

Figure 5: Two example outputs from the BCAT model.

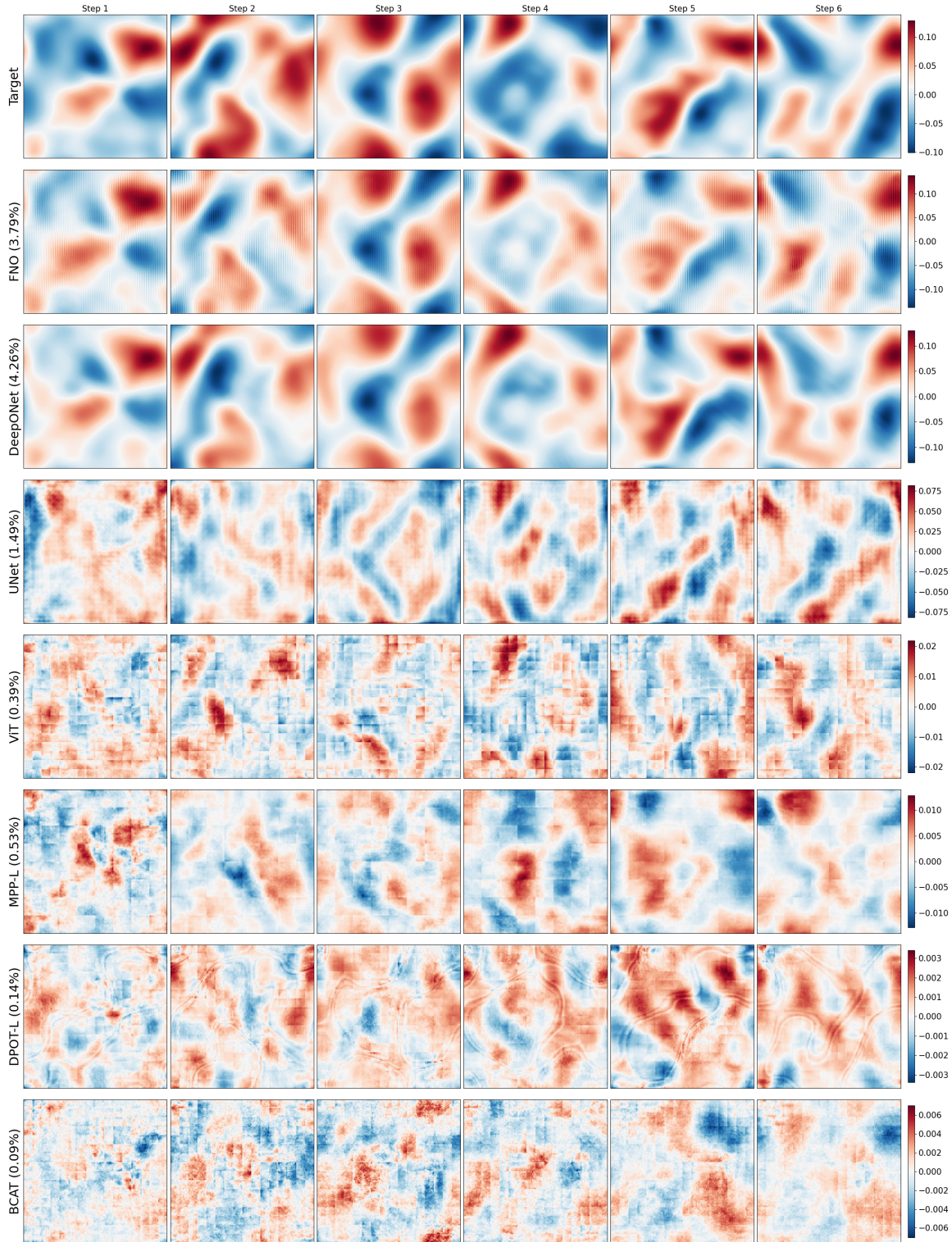


Figure 6: **Comparing outputs from different models.** The target is the first 6 output steps from the PDEBench Compressible Navier-Stokes dataset (y -velocity channel). For each model (each row), we display the difference between target and model output. Relative L^2 errors for the full trajectory are listed after the model names.